First-principles study of Suzuki segregation at stacking faults in disordered face-centered cubic Co-Ni alloys

Dongsheng Wen*, Michael S. Titus

School of Materials Engineering, Purdue University, 701 West Stadium Ave, West Lafayette, IN 47907, USA

Abstract

The formation of stacking faults (SFs) observed in various metallic materials, such as Co-, and Ni-based alloys, influence the plastic deformation and strain-induced phase transformations. One possible explanation for the propensity of SF formation is Suzuki segregation, which is the localized segregation of solute to SFs. Through first-principles calculations, we investigate the driving force of Suzuki segregation in the disordered face-centered cubic Co-Ni binary system and quantitatively predict the resulting temperatureand composition-dependent stacking fault energies (SFEs). We predict the segregation of Co to the stacking fault region in the disordered face-centered cubic Co-Ni binary alloy system utilizing a combination of cluster expansions and Monte Carlo simulations. We find that configurational and vibrational effects aid to stabilize the the SFs through segregation of Co to the two innermost (111) planes in the SFs and predict a reduction of segregation with increasing temperature. We further emphasize that the experimentally determined SFE strongly related to Co segregation and vibrational free energy contributions. The method developed herein could be leveraged to inform alloy design strategies, and predict segregation in other interfacial problems such as grain boundaries and heterointerfaces.

Keywords: interface segregation, stacking faults, Superalloys, density functional theory, thermodynamics

1. Introduction

Stacking faults (SF) form extensively in many transformation-induced plasticity (TRIP) and twinning-induced plasticity (TWIP) face-centered cubic (FCC) alloys, as well as in FCC alloys where partial dislocation decor-

^{*}Corresponding author: wen94@purdue.edu

relation is prevalent [1, 2, 3, 4, 5, 6, 7, 8, 9, 10, 11, 12]. However, minute chemical fluctuations within a few (111) planes from the stacking fault, here referred to as Suzuki segregation are not well understood. Suzuki segregation was proposed in 1952 to explain the increased strength in the Cu-Zn system for intermediate compositions [13, 14] and has been proposed to be driven by thermodynamics [15, 16, 17, 18, 10]. This microscale segregation has profound impacts on macroscopic electronic properties (such as superconducting transition temperature) [19, 20] and mechanical properties (such as creep resistance) [6, 18]. Direct evidence for Suzuki segregation has only recently been gathered in the past twenty years through the efforts of researchers from diverse materials areas [6, 18, 21, 22, 23, 24, 25, 26, 27, 28, 29, 30], and the recent availability of emerging atomic-level resolution techniques, for example, high-resolution high angle annular dark field transmission electron microscopy (HAADF-TEM) and atom probe tomography (APT) [6, 18, 31].

Recent work characterizing solute segregation to stacking faults in metallic alloys has been focused on Ni- and Co-based superalloys, in which solute segregate to the stacking faults in the $\gamma' - Ni_3Al$ and $\gamma' - Co_3(Al, W)$ phases in superalloys [6, 18, 21, 32, 33, 34, 35]. Elemental segregation behavior varies in different alloy classes, and it is not trivial to elucidate the driving forces and trends for segregation due to complex compositions [21, 32]. Early work in Ni-based superalloys from Viswanathan et al. showed that Co atoms segregate to the stacking fault in the $\gamma' - Ni_3Al$ precipitates [32]. Rao et al.'s first-principles study found that Co, Cr, Nb, and Ta showed no driving force of segregation and a more recent study by Feng et al. showed that the segregation of Co atoms stabilizes the Cr segregation at superlattice intrinsic stacking faults (SISFs) [34]. On the Co-rich side, work from Titus et al. showed that the Co content as stacking faults in the $\gamma' - Co_3(Al, W)$ precipitates remains relatively constant, but Ta, W, and Cr segregate strongly to the stacking faults [6]. Additionally, segregation has been strongly correlated to the specific dislocation shearing process of the γ' -precipitates, but the origin of the driving force of segregation is still not fully understood [4, 7, 10, 18].

Despite the efforts made to understand the Suzuki segregation in the aforementioned alloys, there exist knowledge gaps to explain both the driving force of Suzuki segregation and its effect on the resulting stacking fault energy (SFE). Therefore, this work focuses on the disordered FCC Co-Ni binary alloy system so as to provide insight into the driving force for Suzuki segregation and resulting changes to the SFE when stacking faults are introduced in the FCC crystal. We utilize first-principles calculations to predict this behavior, as they have proven to be sufficient to predict segregation in a γ' -strengthened Co-based alloy[18] and predict the driving force for segregation in $\gamma' - Ni_3Al$ [10]. Specifically, we utilize a combination of defect energy calculations,

Ising models, and cluster expansions to quantitatively cross-validate multiple techniques that are able to determine the driving force for segregation and resulting stacking fault energies.

2. Methods

Here we describe the modeling of the ground state unsegregated stacking fault energies with various models in Section 2.1. In Section 2.2, we introduce the methods of modeling of solute interaction energies at the stacking fault, the cluster expansion/effective Hamiltonian method and Monte Carlo simulations to determine solute concentrations. And in Section 2.3, we extend the stacking fault energy calculation to finite temperatures through thermodynamic integration of free energies and stacking fault models. The density functional theory parameters used to perform first-principles calculations are described in Section 2.4. Many additional details are included in the supplementary document.

2.1. Modeling the Unsegregated Stacking Fault

2.1.1. Tilted-cell and Inserted Stacking Fault Models

An intrinsic stacking fault (ISF) in atomistic simulaitons can be created by shearing a perfect periodic FCC crystal whose vertical axis is parallel to the [111] direction within the glide plane. As schematically shown in Figure 1(a), the red dashed box represents the original FCC structure, which is tilted to the blue box by the vector b, producing an intrinsic stacking fault in between. The displacement between the FCC phase and the stacking fault region is characterized by a vector of $b = a/6[\bar{1}\bar{1}2]$ shown in Figure 1(b). Therefore, the primitive supercell of deformed structure can be represented by the tilted-cell in Figure 1(c) with an ISF formed on top of the cell (layer-9). The ground state stacking fault energy (SFE) can be computed by:

$$\gamma_{ISF} = \frac{E_{ISF} - E_{FCC}}{A} \tag{1}$$

where E_{ISF} is the total energy of the tilted stacking fault supercell, E_{FCC} is the total energy of the perfect FCC cell, and A is the area of the interface. The lattice parameters of the FCC and tilted ISF supercells are usually constrained in order to mimic the coherent interface between the FCC and ISF regions.

Apart from the tilted supercell method in Figure 1(c), E_{ISF} can also be calculated by inserting the stacking fault planes in the FCC matrix. This is illustrated by the black box in Figure 1(a) and Figure 1(d). In this case,

the ISF is inserted to the FCC matrix while the supercell remains straight along c-axis. In Figure 1(d), the 5^{th} and 6^{th} planes are considered as the intrinsic stacking fault. It is important to note that the tilted cell models have 3n layers while the inserted ISF supercells have 3n-1 layers, where nis an integer representing the number of repeating ABC (111) layers in a perfect FCC crystal. Convergence tests of the volume of these two methods were carried out by varying n, the repeating FCC-(111) ABC planes, and we found that just 9 and 8 total (111) layers were sufficient to calculate the stacking fault energy, as shown in the Result section. The calculation details of convergence tests are enclosed in the supplementary Section 1. For consistency and convenience throughout the paper, "FCC+ISF" is used exclusively for the inserted supercell shown in Figure 1(d). For these two methods, it is important to choose the correct ideal FCC structure for E_{FCC} . Inaccurate stacking fault energies can be determined by choosing the problematic reference energy. For the inserted FCC+ISF supercell with 3n-1 layers, there is no direct FCC supercells with the same number of layers and the E_{FCC} is calculated by $(3n-1)e_{FCC}$, in which e_{FCC} is expressed as energy per layer calculated for a perfect FCC structure [36]. Li et al have shown that with increasing number of layers in the supercell, the interactions due to the periodic boundary conditions can be mitigated [36]. In this study, we showed that n=3 is sufficient to calculate the ISFE of pure Co and Ni.

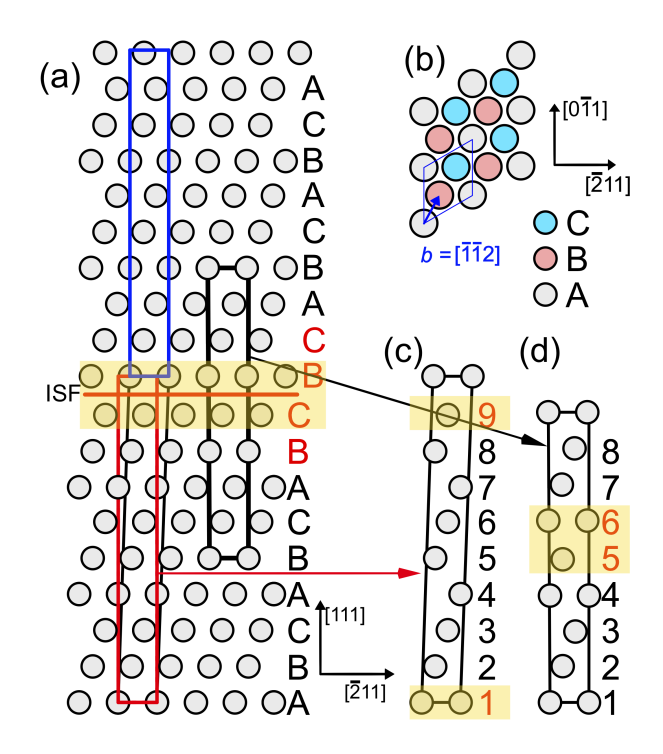


Figure 1: Schematics of creating intrinsic stacking fault supercells. (a) Stacking sequence of the intrinsic stacking fault. (b) Displacement vector $b = a/6[\bar{1}\bar{1}2]$ for creating an intrinsic stacking fault in the FCC structure. (c) The tilted supercell where layer-1 and layer-9 are ISF planes. (d) The nserted FCC+ISF supercell where layer-5 and layer-6 are ISF planes.

2.1.2. Axial Nearest Neighbor Ising Model

In addition to the SFE calculated through Eq.1, we also utilized the axial nearest-neighbor Ising model (ANNI) [37, 38]. This model has the advantages of reducing the computational cost and allowing reasonable results for a variety of systems [38, 39, 40]. The ANNI SFE is expressed by:

$$\gamma_{ISF}^{ANNI} = 2 \frac{e_{HCP} - e_{FCC}}{A} \tag{2}$$

where e_{HCP} is the total energy per atom of the HCP supercell, e_{FCC} is the energy per atom of the FCC supercell, and A is the calculated area of the (111)-FCC plane per atom. This method is usually more computationally-convenient because of smaller supercells compared with tilted supercells and FCC+ISF supercells.

Primitive 1-atom FCC and 2-atom HCP cells were fully relaxed to calculate the SFE for pure Co and Ni. For the FCC cell, the conventional lattice parameter is a=3.52Å. For the HCP cell, the conventional lattice parameters are a=2.49Å and c=4.17Å.

5 2.2. Modeling the Segregation Behavior at the Stacking Fault

The Co-Ni system is well-known to form FCC solid solution, but how solutes interact with the ISF has yet to be clearly understood. Here we describe the methods to model driving force of stacking fault segregation and equilibrium concentrations.

2.2.1. Interaction Energy

When Co is added to the FCC Ni with an ISF, the interaction energy can be expressed layer-by-layer for a Co atom replacing a Ni lattice site on the planes. This interaction energy, defined in a previous study of Ni-based superalloys, is given by [10]:

$$\Delta \gamma_{ISF}^{i,Co} = \frac{E_{ISF}^{i,Co} - E_{FCC}^{i,Co}}{A} - \gamma_{ISF} \tag{3}$$

where $E_{ISF}^{i,Co}$ and $E_{FCC}^{i,Co}$ are the ground state total energies obtained from replacing a Ni atom by a Co atom in the i^{th} -layer of the tilted supercell and FCC supercell shown in Figure 1(c), and γ_{ISF} is the stacking fault energy described in Eq(1). This interaction energy is able to semi-qualitatively determine the driving force of segregation via the sign of the value; solute segregation is expected for negative interaction energies, while depletion is expected for positive interaction energies [10]. We used the 9-layered tilted supercells in Figure 1(c) and their corresponding FCC supercells. In addition, to understand the interaction energy with respect to Co concentrations, we used three different volumes of the 9-layered supercells: volume-1 (1 × 1 × 1, 9 atoms), volume-2 (2 × 2 × 1, 18 atoms), volume-4 (2 × 2 × 1, 36 atoms). By replacing one Co atom at a time, the Co concentrations for the volume-1, volume-2, and volume-4 are 11.11 at.%, 5.56 at.%, and 2.78 at.%, respectively. The same methods were employed to investigate interaction energy of Ni on FCC Co.

2.2.2. 0 Kelvin Cluster Expansion

The interaction energy is a first-order approximation in the dilute region of the Co-Ni alloy, but we are more interested in modeling the solute segregation for the whole concentration range. The concentrated compositions have high degrees of freedom in a complicated supercell and therefore, cluster expansion (CE) was utilized to aid our study. We utilized the 8-layered FCC+ISF supercell defined in Figure 1(d). A Clusters Approach to Statistical Mechanics (CASM) software [41] was utilized to enumerate all the possible configurations with the supercells up to three-volume (24 atoms) of the 8-layered supercell. The enumerated supercell structures are shown in

Figure 2: v-1, v-2, v-3_1 and v3_2 have 8, 16, 24, and 24 atoms, respectively. More than three millions symmetrically-distinct configurations were enumerated. For a given configuration, we referenced the ground state formation energy by:

$$E_f^i = E_0^i - E_0^{Co} X_{Co} - E_0^{Ni} X_{Ni} (4)$$

where E_0^i is the total energy of configuration i, X_{Co} and X_{Ni} are the Co and Ni concentrations for this configuration, and E_0^{Co} and E_0^{Ni} represent the total energy of pure Co in HCP structure and pure Ni in FCC structure. Because configurations can have different cell volumes, all energies in Eq(4) are normalized in terms of the primitive cell. A finite set of configurations were used to train the cluster expansion, given by [42, 43]:

$$E_f(\vec{\sigma}) = J_0 + \sum_i J_i V(\vec{\sigma}_i) + \sum_{i,j} J_{ij} V(\vec{\sigma}_{ij}) + \sum_{i,j,k} J_{ijk} V(\vec{\sigma}_{ijk}) + \sum_{i,j,k,l} J_{ijkl} V(\vec{\sigma}_{ijkl})$$
(5)

where $E_f(\vec{\sigma})$ is the cluster expansion formation energy, $V(\vec{\sigma}) = V(\{\sigma_1, ...\sigma_n\})$ is the basis function of a given configuration, and σ_i is the occupation variable of a lattice site, which takes +1 when it is occupied by a Co atom, or -1 when it is occupied by a Ni atom. J_i , J_{ij} , J_{ijk} , and J_{ijkl} , are the effective cluster interactions (ECIs) of point, pair, triplet, and quadruplet clusters that are used to fit the basis function with the first-principles formation energies. A genetic algorithm coupled with a K-fold cross-validation (CV) scheme was employed to train the cluster expansion [44, 43, 45]. The cross validation parameter was used as the objective function, and it is given by:

$$CV = \frac{\sum_{i=1}^{n} (E_f^i - \tilde{E}_f^i)^2}{N}$$
 (6)

where E_f^i and \tilde{E}_f^i are the ab-initio and predicted formation energy of configuration i, respectively, and N is the number of selected configurations in the fitting. More details of the training processes are described in the supplementary Section S2.

We also utilized the above methods to fit CEs to a 1-atom FCC and 2-atom HCP primitive cell. Up to 16-volume and 8-volume supercells were enumerated, respectively.

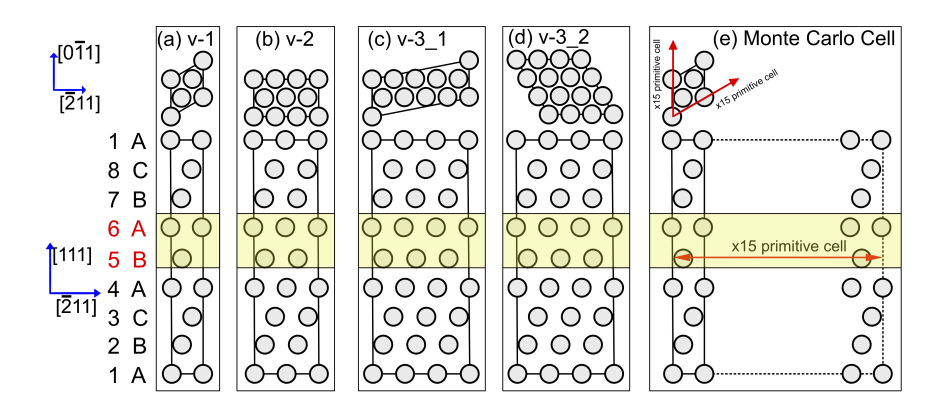


Figure 2: Supercells for configuration enumeration and Monte Carlo simulation. (a) 1-volume supercell, (b) 2-volume supercell, (c) 3-volume supercell type-1, and (d) 3-volume supercell type-2 are used in configuration enumeration. (e) $15 \times 15 \times 1$ supercell used in semi-grand canonical Monte Carlo simulations.

2.2.3. Semi-Grand Canonical Monte Carlo Simulation

Thermodynamic properties of the Co-Ni system in FCC+ISF, FCC, and HCP were evaluated by semi-grand canonical ensembles Monte Carlo (GCMC) simulations. The major statistical mechanics formulations and applications can be found in previous studies [43, 46, 47]. In this study, we mainly focused on evaluating the equilibrium composition of stacking fault in the FCC+ISF supercell. The averaged composition of each (111) atomic plane in the 8layered supercell was evaluated at a constant temperature in order to compare the compositions between the stacking fault region and FCC region. For the FCC+ISF structure, the GCMC simulation cell contains $15 \times 15 \times 1$ 8-atom supercells, as shown in Figure 2(e). For FCC and HCP structures, the GCMC cells contain $15 \times 15 \times 15$ of the FCC and HCP primitive cells. Thermodynamic properties, such as grand potential, formation energies, ensemble average, and planar equilibrium concentrations were evaluated from 200K to 1500K with an increment of 10 K. The GCMC parameters and conditions are detailed in the previous studies [43, 47] and the supplementary Section S3.

2.3. Finite Temperature Contributions to Stacking Fault Energies

2.3.1. Thermodynamic Integration

The free energies for FCC+ISF, FCC, and HCP structures at finite temperatures were evaluated through thermodynamic integration. The Gibbs free energy of a phase ϕ (ϕ is FCC+ISF, FCC, or HCP) at a given temper-

ature and composition can be constructed by the following equation:

$$g_{\phi}(T, X_{Co}) = e_{\phi}^{0} + g_{\phi}^{conf.}(X_{Co}) + g_{\phi}^{vib.}(X_{Co})$$
 (7)

in which e_{ϕ}^{0} is the ground state energy of phase ϕ referenced to the stable structure; in this case, Ni is referenced to FCC and Co is referenced to HCP. $g_{\phi}^{conf.}(X_{Co})$ is the configurational contribution, and $g_{\phi}^{vib.}(X_{Co})$ is the vibrational contribution. $g_{\phi}^{conf.}(X_{Co})$ can be obtained from the GCMC simulation results through thermodynamic integration, the theoretical formulations of which are described in previous studies [43, 46, 47]. The vibrational part was calculated by compositionally-weighted vibrational free energy of pure Co and Ni for a given structure ϕ :

$$g_{\phi}^{vib.}(X_{Co}) = g_{\phi}^{vib.,Co} X_{Co} + g_{\phi}^{vib.,Ni} (1 - X_{Co})$$
(8)

The vibrational free energies of Co and Ni in different structures were calculated via the quasi-harmonic approximation (QHA) implemented in the *phonopy* software [48, 49]. More details of these calculations are provided in the Section S4 in the supplementary.

2.3.2. Extension of ANNI to Finite Temperature

190

195

With the Gibbs free energy of FCC and HCP structure, we first extend the ANNI model to calculate the stacking fault energy:

$$\gamma_{ISF}^{ANNI}(T,X) = 2 \frac{g_{HCP}(T,X) - g_{FCC}(T,X)}{A_{\{111\}}(T,X)} \tag{9}$$

where $A_{\{111\}}(T, X)$ is the area per atom of the (111) glide plane; it can be calculated by compositionally-weighing the glide plane area of pure Ni and Co in FCC structure at elevated temperatures, which can be calculated from the QHA thermal expansion.

2.3.3. Ericsson Model for Segregated Stacking Faults

For the FCC+ISF model, we adopted Ericsson's treatment to calculate the SFE with and without segregation [15, 16]. Based on Ericsson, the free energy of an FCC material containing an intrinsic stacking fault can be described by:

$$g_{FCC+ISF}(X_{tot}) = n_{FCC}g_{FCC}(X_{FCC}) + n_{ISF}g_{ISF}(X_{FCC}, X_{ISF})$$
(10)

where $g_{FCC+ISF}(X_{tot})$ is the molar free energy of the whole system with an averaged composition X_{tot} , n_{FCC} and n_{ISF} are the number of moles in the FCC and ISF region, $g_{FCC}(X_{FCC})$ is the molar free energy of the FCC region with an equilibrium concentration X_{FCC} , and $g_{ISF}(X_{FCC}, X_{ISF})$ is the molar free energy of the FCC region with an equilibrium concentration X_{ISF} . The ISF phase can be seen as a plate-like HCP structure containing two or more atomic planes according to the geometry and composition of the faulted region [15]. For example, the 5^{th} and 6^{th} planes of the 8-layered FCC+ISF supercell in Figure 1(d) are considered the ISF phase separating the FCC phase. In this case, the ratio between n_{FCC} and n_{ISF} is 3:1. The graphical illustration provided by Ericsson is adopted in Figure 3, in which the free energy curves are shown for FCC (red curve) and ISF (blue curve) phase. At equilibrium, the Suzuki segregation criterion [13] is achieved by the equivalence of the FCC exchange potential evaluated at X_{FCC} and the ISF exchange potential evaluated at X_{ISF} :

$$\mu_{FCC}^{Ni}(X_{FCC}) - \mu_{FCC}^{Co}(X_{FCC}) = \mu_{ISF}^{Ni}(X_{ISF}) - \mu_{ISF}^{Co}(X_{ISF})$$
 (11)

where μ_i^j is the chemical potential of species j (Co or Ni) in the i=FCC or ISF structures, and X_i is the equilibrium concentration in the i= FCC or ISF. This relationship is graphically shown by the red and blue dashed lines in Figure 3. According to Ericsson, when one mole of ISF phase with composition X_{ISF} is formed from the FCC matrix with composition X_{FCC} , the stacking fault energy is:

$$\gamma_m(X_{FCC}, X_{ISF}) = g_{ISF}(X_{FCC}, X_{ISF}) - \mu_{FCC}^{Co}(X_{FCC})X_{ISF} - \mu_{FCC}^{Ni}(X_{FCC})(1 - X_{ISF})$$
(12a)

$$g_{ISF}(X_{FCC}, X_{ISF}) = g_{FCC}(X_{ISF}) + \epsilon(X_{FCC}, X_{ISF}) + \omega(X_{ISF})$$
 (12b)

The stacking fault energy calculated by Eq.(12) naturally includes two energy contributions envisioned by Ericsson [15]. The first term is $\epsilon(X_{FCC}, X_{ISF})$, the interface energy due to chemical fluctuation between the ISF and FCC. And the second term is $\omega(X_{ISF})$, known as the energy due to structural change by an ISF in the FCC medium. Assuming no segregation, $X_{ISF} = X_{FCC}$, and there will be no interface energy resulting from chemical fluctuation. From this derivation, we can calculate the segregated or unsegregated stacking fault energy. A detailed description is provided in the Appendix for SFE calculations and required quantities.

It is important to note that $\gamma_m(X_{FCC}, X_{ISF})$ is expressed as energy per mole of ISF and should be converted to the commonly used "energy per unit area". The stacking fault interface can be seen between the innermost planes

(the 5^{th} and 6^{th} planes), indicating that the ISF phase contains two moles. Therefore, for one mole of stacking fault in Eq.(12), the area should be half of the (111) glide plane area A_{111} :

$$\gamma(X_{FCC}, X_{ISF}) = \frac{2\gamma_m(X_{FCC}, X_{ISF})}{A_{\{111\}}(X_{FCC})}$$
(13)

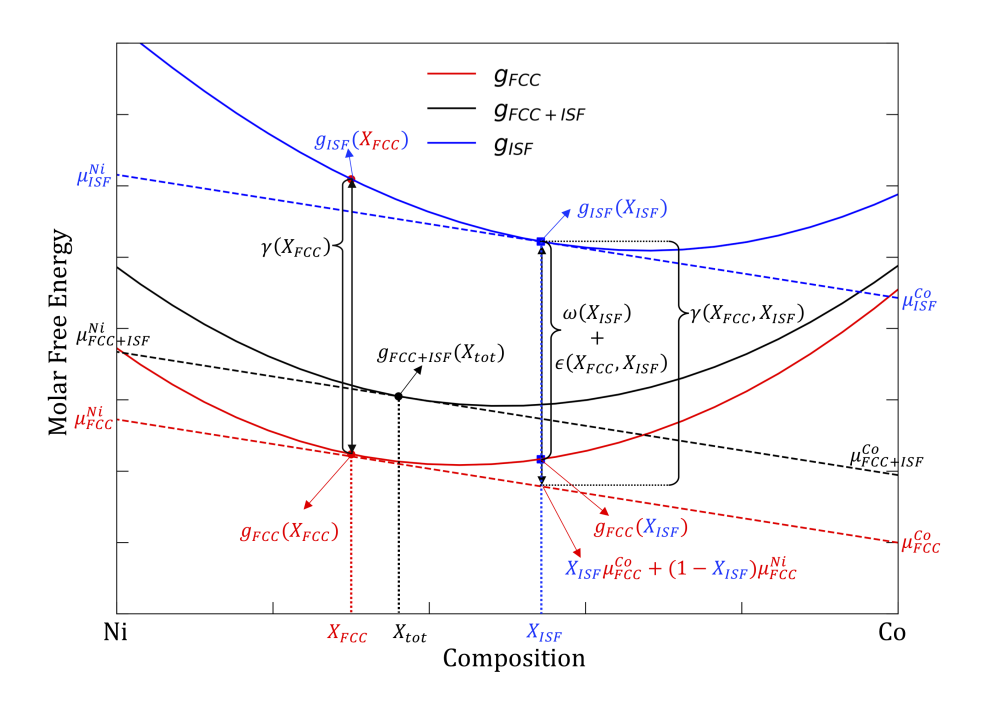


Figure 3: Graphical illustration of the relations between free energies of FCC and ISF phases at equilibrium. Adapted from Ref.[15].

2.3.4. First-Principles Calculation Parameters

Density functional theory calculations were performed to calculate the ground state total energies of various supercells introduced in the above sections, using the Vienna Ab-initio Simulation Package (VASP) [50, 51, 52]. The local interactions between ions and electrons were modeled using the Projector Augmented-Wave method [53]. The approximation of the exchange-correlation energy was calculated by the Generalized Gradient Approximation (GGA) parameterized by Perdew, Burke, and Ernzerhof [54]. Colinear spin-polarization was considered for all supercells, and the initial magnetic moments for Co and Ni were set to 2 and 1 μ_B . The plane wave energy cut-off of all elements was set to 400 eV. The k-point meshes for various supercells were determined by the Monkhorst-Pack scheme [55] with a Γ -centered k-point density equivalent to $31 \times 31 \times 31$ per FCC primitive cell.

The Methfessel-Paxton smearing method was used to perform the reciprocal-space energy integration with a smearing width of 0.2 eV [56] for the structural relaxation. Ionic and cell volume/shape relaxations were carried out before highly-accurate static calculations. For the static calculations of total energies, no volume/ionic changes were allowed. The tetrahedron method with the Blöchl correction [57] was used to replace the Methfessel-Paxton smearing method for energy integration. The electronic self-consistent loops were considered converged when the difference of total energies between two steps fell bellow 1×10^{-4} eV per cell for FCC, HCP, and FCC+ISF supercells. For the interaction energy calculations in Section 2.2.1, in order to constrain the lattice parameters in the tilted supercells, the shearing burgers vector was added to the fully converged FCC supercells to create the tilted supercells. Afterwards, only ionic relaxations were allowed for the tilted supercells while keeping the cell volume constant.

3. Results

3.1. 0 Kelvin SFEs and Interaction Energy

Figure 4 presents the 0 K SFE of pure Co and Ni calculated by three different methods: tilted supercells, inserted FCC+ISF supercells, and ANNI methods. The SFE of pure Ni is between 125 to 135 mJ/m^2 (see Figure 4(b)), and it agrees very well with the reported values between 110 to 150 mJ/m^2 by various first-principles methods [36, 58] and the well-known experimental data between 120 to 130 mJ/m^2 [59]. The SFE of pure Co ranges between -120 to -100 mJ/m^2 (see Figure 4(a)) and agrees with the previous DFT calculated -105.6 mJ/m^2 [60]. Achmad et al. calculated the SFE for FCC Co with a similar method but the values were close to zero [61]. This is because they chose an 11-layered structure to calculate FCC energy, which is inappropriate due to an unintended stacking fault embedded in the FCC supercell [61]. Both tilted supercells and inserted FCC+ISF supercells have shown good convergence with various number of layers in the supercells. The ANNI model predicts an SFE of 143 mJ/m^2 for Ni and a value of -110 mJ/m^2 for Co, as shown as dashed lines in Figure 4(a) and Figure 4(b). Therefore, the 9-layered tilted supercell in Figure 1(c) and 8-layered inserted FCC+ISF supercell in Figure 1(d) are eligible to be used to investigate the solute behaviors of both Co-based and Ni-based alloys.

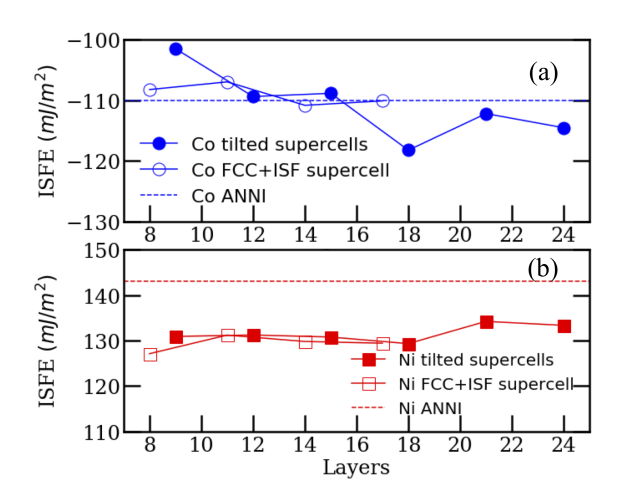


Figure 4: Calculated stacking fault energies for (a) Co and (b) Ni with tilted supercells, FCC+ISF supercells, and ANNI methods.

The calculated interaction energy of Co in Ni-rich compositions was determined to be negative in layers 1 and 9, as shown in Figure 5, which represent the layers within the ISF (Figure 1(c)). The negative interaction energy implies that a driving force exists at 0 K for Co to segregate to the ISF. Therefore, we expect that Co would segregate to the ISF across the Co-Ni system.

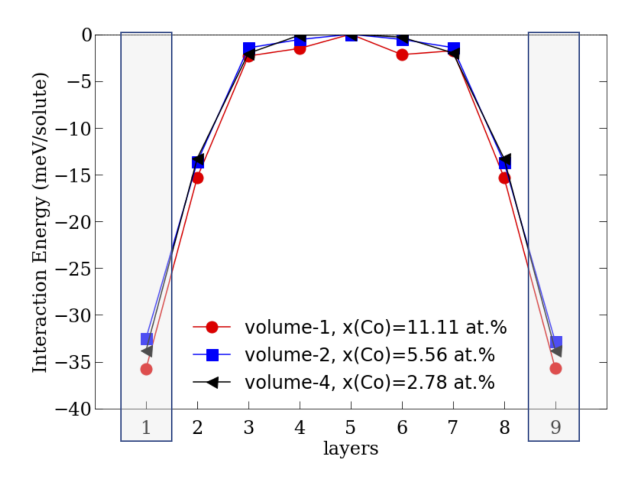


Figure 5: Co interaction energies vs. single atomic layer in FCC Ni, calculated using the tilted supercell method.

3.2. Cluster Expansion and Effective Cluster Interactions

275

The CE exhibited a CV value of 0.78 meV/atom, below the expected DFT convergence error (usually 1 meV/atom). The root mean square error

(RMSE) of the best fit is 0.74 meV/atom for all the reported configurations. The ECIs of the best fit are shown in Figure 6(b).

For the 7667 CE-predicted FCC+ISF structures at $Co_{50}Ni_{50}$, the total energies of supercells slightly decreases in 3-volume supercells, as shown in Figure 7(a) where the averaged energy of 24-atom supercells is about 0.001 eV/atom lower than the energies of 8-atom and 16-atom supercells.

More importantly, the energies of Co₅₀Ni₅₀ supercells decrease with increasing Co occupations in the ISF planes, as seen in Figure 7(b) where the x-axis is the ratio between the number of Co atoms on the ISF planes $(N_{ISF}(Co))$ and the total number of atoms in the supercell (N_{tot}) . For the supercells with higher Co occupations on ISF planes $(N_{ISF}(Co)/N_{tot} = 0.2083)$ and 0.25), the averaged energy is about 5 meV/atom lower than the averaged line. A trend of decreasing energy with increasing Co content at the fault can be observed in Figure 7(b). Furthermore, we have constructed and calculated the DFT energies of 23 special quasi-random structures (SQS) [62, 63] for the $Co_{50}Ni_{50}$ composition. SQSs have been used to mimic the disordered distribution of solutes in Co-, and Ni-based alloys for stacking fault energies [58, 6, 64, 65]. In this study, 11 32-atom supercells $(2 \times 2 \times 1)$ of the 8-layered cell) and 12 48-atom $(2 \times 3 \times 1)$ SQS supercells were calculated using the same DFT procedures/parameters in Section 2.3.4, more details of the SQSs are provided in Section S5 in the supplementary document. The DFT energies of the SQSs are shown in Figure 7(b) that the averaged value is -6.2493 eV/atom. The above observations suggest a 0 K driving force of Co segregation in the ISF.

For the FCC structure, the formation energies and ECIs are shown in Figure 6(c) and Figure 6(d), and both the CV score and RMSE of the fit are 0.8 meV/atom. The formation energies and ECIs of the binary system in HCP structure are provided in Figure 6(e) and Figure 6(f). A very good fit was achieved with a CV score of 1.03 meV/atom and a RMSE of 0.95 meV/atom.

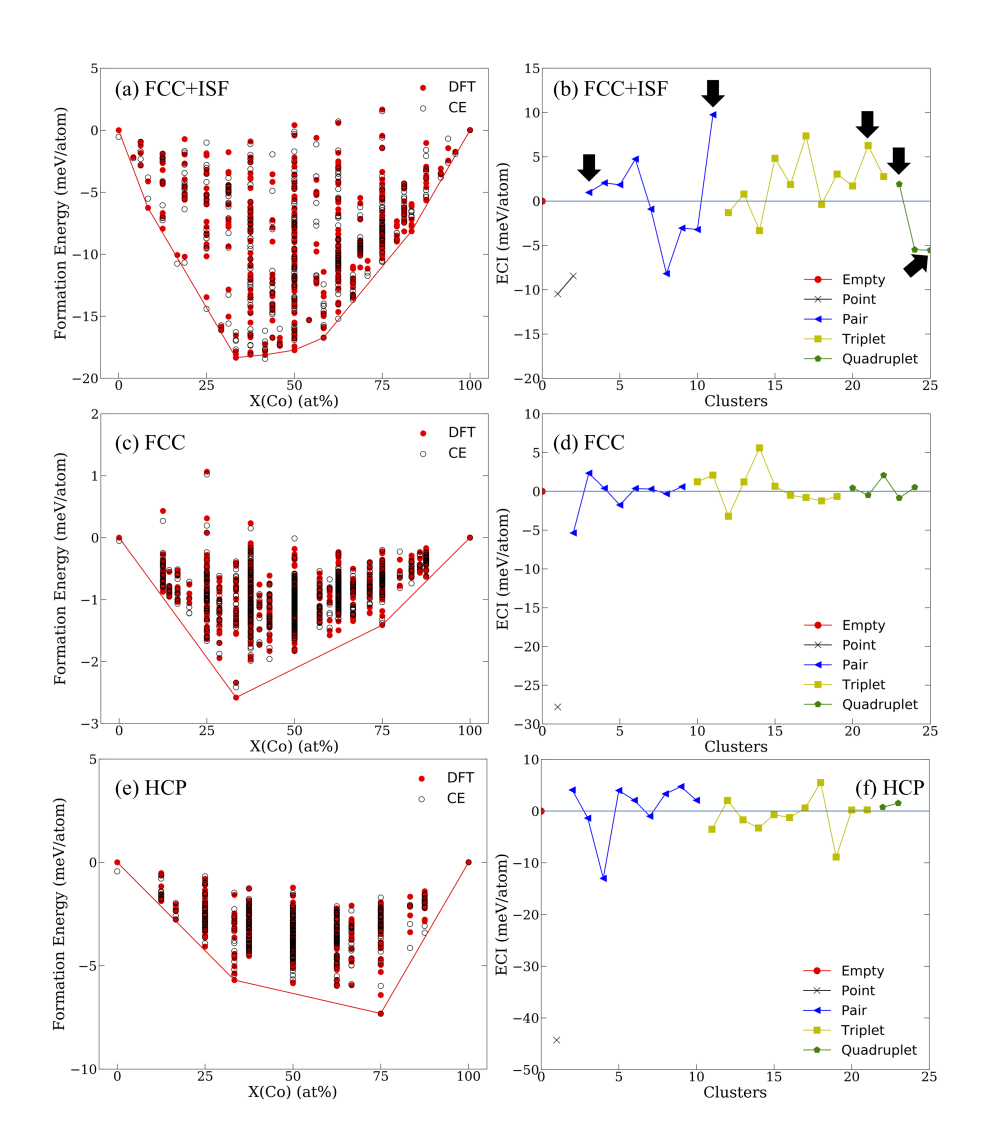


Figure 6: FCC+ISF: (a) DFT calculated and CE predicted formation energies of Co-Ni FCC+ISF structure. (b) Effective cluster interactions (ECI) of the best fit of FCC+ISF where black arrows represent interactions between stacking fault atoms and FCC atoms. FCC: (c) DFT calculated and CE predicted formation energies of Co-Ni FCC structure. (d) ECI of the best fit of FCC structure. HCP: (e) DFT calculated and CE predicted formation energies. (f) ECI of the best fit of HCP structure.

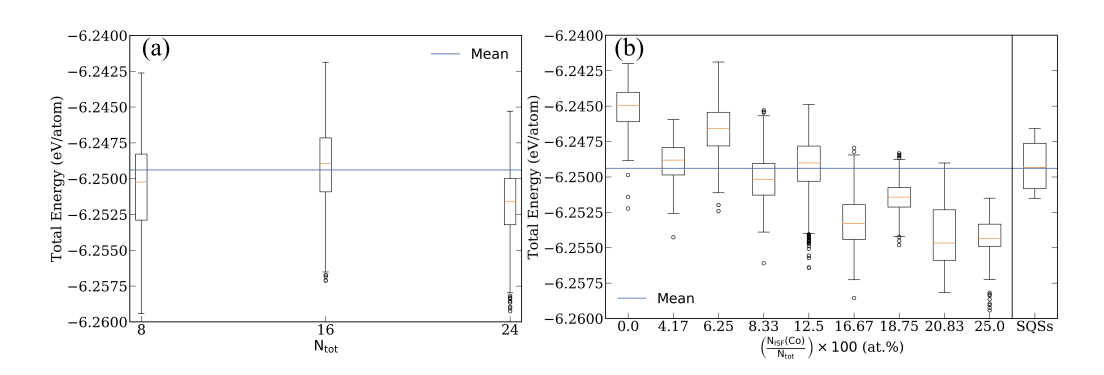


Figure 7: 0 K total energies of all the CE-predicted configurations at the composition of $\text{Co}_{50}\text{Ni}_{50}$ for the FCC+ISF structure: (a) Energy vs. number of atoms in the supercells. (b) Energy vs. $\frac{N_{ISF}(Co)}{N_{tot}}$ where $N_{ISF}(Co)$ is the number of Co atoms in the two-layered ISF and N_{tot} is the total number of atoms for a configuration. The last column in (b) corresponds to DFT-calculated energies of 23 FCC+ISF SQSs for $\text{Co}_{50}\text{Ni}_{50}$.

3.3. Segregation Behavior of FCC+ISF Structure

Co was predicted to always segregate to the innermost two planes of the ISF across all FCC matrix compositions at 900°, as shown by the GCMC simulations in Figure 8(a). Co segregation was predicted in the ISF planes of the supercell while the Co concentrations in the other FCC planes remained largely unchanged. The Co enhancement is almost entirely confined to the two innermost (111)-planes, corresponding to the negative Co interaction energy in the ISF-planes (see Figure 5). The segregation behavior is schematically marked on the Co-Ni binary phase diagram at 900°C, see Figure 8(b). The closed symbols along the 900°C represent the FCC composition and open symbols represent the ISF composition.

The extent of Co segregation was predicted to be the greatest at near 50-50 compositions, and it monotonically decreased to 0 for pure Ni and Co, as shown in Figure 8(c). With increasing temperatures, a reduced segregation was observed following an Arrhenius-like behavior which will be discussed in Section 4.3.

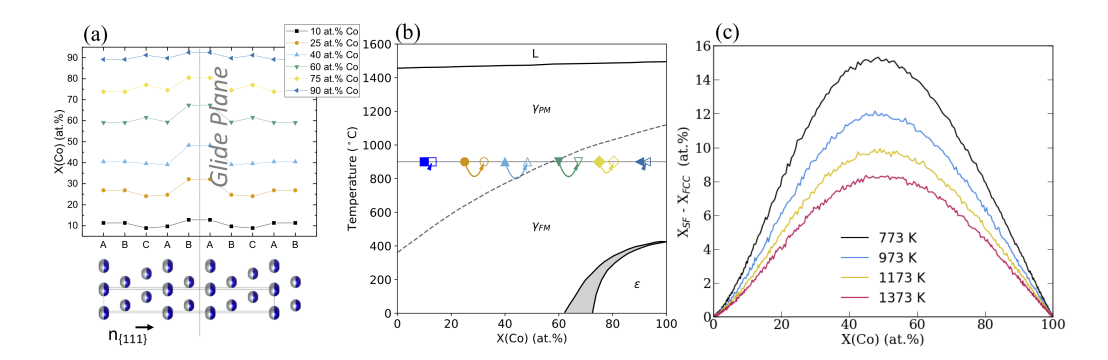


Figure 8: (a) Co concentration vs. position in the supercell, where each series is the average Co composition in the FCC matrix regions (ABCA..BC, where .. represents the two SF planes). Co is observed to always segregate to the SF, regardless of composition. (b) Average matrix and SF compositions of the Co-Ni alloy at 900°C mapped onto the Co-Ni binary phase diagram show that the SF composition deviates from its matrix and moves towards Co. Closed markers are for matrix composition, open markers are for SF composition, markers with the same shape are for one composition. (c) The extent of Co segregation with increasing Co concentration at 773 K, 973 K, 1173 K, and 1373 K predicted by Monte Carlo simulations.

3.4. Stacking Energy at Finite Temperatures

3.4.1. ANNI SFE at Finite Temperatures

335

For pure Co, the ANNI SFE increased from -75 mJ/m^2 at 0 K to 44 mJ/m^2 at 1500 K, see grey line in Figure 9. The HCP-to-FCC transformation temperature for Co was about 925 K (see Figure 9 where the Co SFE is zero), this transformation temperature was higher than the experimental data of 700 K (see Figure 8(b)). The ANNI SFE of Ni decreased monotonically from 116 mJ/m^2 at 0 K to 62 mJ/m^2 at 1500 K (as shown in Figure 9), which agreed with the first-principles calculations of Ni SFE were reported in Zhang et al.'s study [38]. Quasiharmonic phonons was the major contribution to the reduction of Ni SFE [38] and it was expected to be the major contribution to the increase of Co SFE.

For Co-Ni alloy compositions at 570 K, the ANNI model predicted a decrease of SFE from 140 mJ/m^2 to -110 mJ/m^2 with increasing Co concentrations when only g_{ϕ}^{conf} was considered for finite-temperature entropic effects, see red line with open-square markers Figure 10(a). When g_{ϕ}^{vib} was also considered, the ANNI SFE decreased from 92 mJ/m^2 to -55 mJ/m^2 at about 82.5 at.% and then slightly increased to -33 mJ/m^2 for pure Co, as shown in red-closed-circles in Figure 10(a). Phonon vibrational effects reduced the SFE in the Ni-rich region and raised the SFE in the Co-rich region.

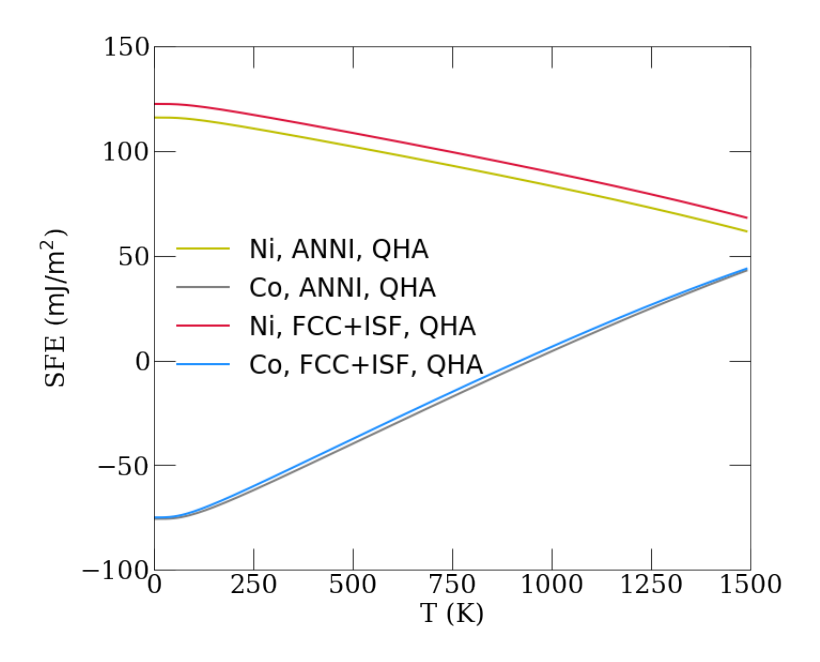


Figure 9: Stacking fault energy of pure Co and Ni at finite temperatures.

3.4.2. Ericsson SFE at Finite Temperatures

For pure Co in FCC+ISF structure, SFE increased from -75 mJ/m^2 at 0 K to 44 mJ/m^2 at 1500 K, which was almost identical to the ANNI result (see Figure 9). For Ni in FCC+ISF, the SFE dropped from 125 mJ/m^2 at 0 K to 70 mJ/m^2 , following the same trend as ANNI SFE of Ni. About an 8 to 9 mJ/m^2 difference was observed between the FCC+ISF Ni (red line) and ANNI Ni (yellow line) in Figure 9.

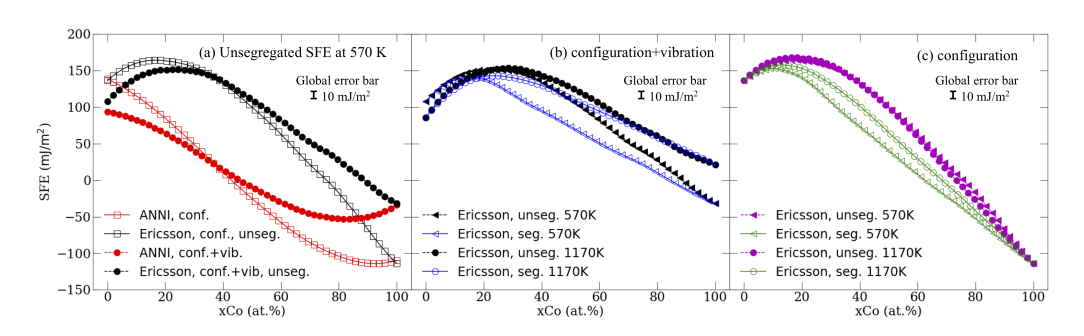


Figure 10: (a) Unsegregated stacking fault energies of Co-Ni alloy at 570 K and 1170 K predicted by the ANNI model and the Ericsson model. (b) Segregated and unsegregated stacking fault energies of Co-Ni alloy at 570 K and 1170 K predicted by the Ericsson model, considering the configurational and the vibrational contributions. (c) Segregated and unsegregated stacking fault energies of Co-Ni alloy at 570 K and 1170 K predicted by the Ericsson model, considering only the configurational contribution.

The SFEs predicted by the Ericsson model exhibited different trends from the ANNI SFEs. Both unsegregated and segregated SFEs predicted by the Ericsson model first increased with Co concentration from 0 to about 20 at.% and then decreased monotonically to 100 at.% (Figure 10).

For the unsegregated SFE at 570 K, the g_{ϕ}^{vib} contribution reduced the SFE of Ni-rich alloys and increased the SFE of Co-rich alloys, comparing the SFEs calculated by $g_{\phi}^{conf} + g_{\phi}^{vib}$ and by g_{ϕ}^{conf} in Figure 10(a).

The segregated SFEs were observed to be lower than the unsegregated SFEs for the whole composition range at 570 K and 1170 K, as shown in Figure 10(b) and Figure 10(c). By considering only the g_{ϕ}^{conf} , the unsegregated SFEs at both 570 K and 1170 K exhibited minor differences. The segregated SFEs at 570 K, however, was always lower than that at 1170 K.

To clarify these differences, the energy difference between the segregated and unsegregated states (denoted as SFE^{seg} - SFE^{unseg}) are shown in Figure 11. This energy difference was 0 for pure Ni and Co, and was observed to be negative for the concentrated compositions. Three main observations can be made: (1) The energy difference between the segregated and unsegregated SFEs decreased with increasing Co content up to around 50 at.% and then increased to 0 at 100 at.%, (2) the energy difference was reduced when temperature increased, observed by comparing the red and blue curves for 570 K and 1170 K in Figure 11, and (c) when both configurational and vibrational effects were considered, the difference in stacking fault energies (SFE^{seg} - SFE^{unseg}) was reduced, compared to the energy difference when only configurational effects were considered (see red lines in Figure 11(a) and (b) for 570 K, same for blue lines for 1170 K).

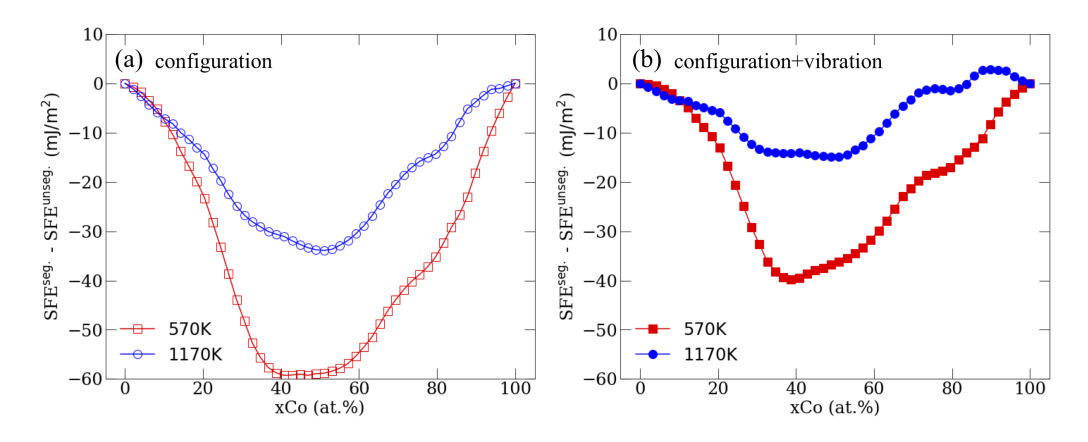


Figure 11: Difference in stacking fault energies between segregated and unsegregated stacking faults predicted by the Ericsson model, (a) considering only the configurational effects, and (b) considering both the configurational and vibrational effects.

To compare the current model with the experimental data, we calculated the SFEs of Co-33Ni alloy to compare with experimental data over temperature [66]. Good agreement was calculated between the Ericsson segregated SFE and experimental data, as shown in Figure 12. Both experimental and predicted data show an increase of SFE at elevated temperatures. At 583 K, the segregated SFE is about 38 mJ/m^2 , higher than the experimental data of 20 mJ/m^2 . At 823 K, the segregated SFE is about 62 mJ/m^2 , also higher than 32 mJ/m^2 measured by Ericsson [66]. The unsegregated SFEs were higher than the experimental values, and the ANNI model underestimated by more than 50 mJ/m^2 compared to the Ericsson model for this composition.

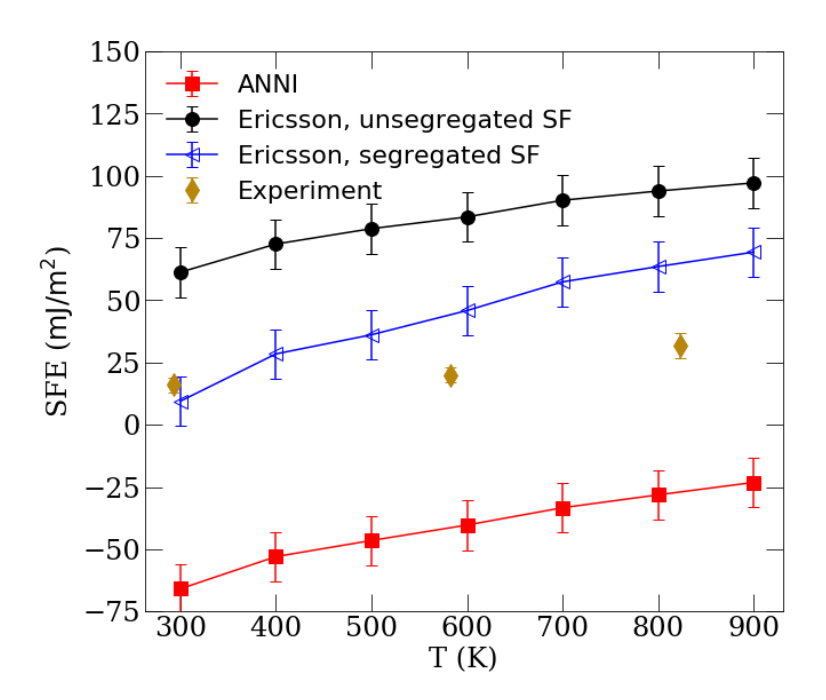


Figure 12: Stacking fault energy of pure Co and Ni at finite temperatures. All the predictions include both phonon vibration and configuration contributions. The experimental data is adapted from Ericsson's work [66].

3.4.3. Sources of Error in SFE Calculations

The main source of uncertainty for the Ericsson FCC+ISF treatment could be from the underlying assumption in the treatment of Eq.(10) - that the compositions of the ISF and FCC are considered homogeneous. If the segregation behavior extent to the FCC planes in the vicinity of ISF planes, such an assumption may need be invalid, and a discrete model may be applied [15]. In fact, the predicted compositions across the FCC layers (Figure 8(a))

exhibit only slight deviations from the averaged composition. Therefore, such trivial deviation was unlikely to cause problems in this study.

Other influences on the SFEs were included in the error bars. This error mainly included corrections from interlayer interactions and constrained lattice parameters [36]. Li et al. showed that interactions between ISF layers in the periodic cell along [111] direction causes difference in SFE calculation. They found that the interface interaction for pure Ni is -4.4 mJ/m^2 for an 11layered inserted FCC+ISF supercell [36]. We expected a small uncertainty value for the 8-layered FCC+ISF supercell in our study, on the order of 5 mJ/m^2 based on Figure 4. Another source of error arises from the changed in elastic energy at a coherent boundary between FCC and ISF. It is more reasonable that the interatomic spacing between ISF atoms are constrained by the FCC phase. As mentioned in the Method section, the tilted supercells are constrained to maintain the same lattice parameters as the FCC cells in order to capture this strain energy. But all the configurations in HCP, FCC, and 8-layered FCC+ISF models were fully relaxed in the DFT calculations. Comparing the SFEs between the tilted supercell method and FCC+ISF in Figure 4, it is reasonable to expect a strain energy correction up to $5 mJ/m^2$. Therefore, a universal error bar of $\pm 10 \ mJ/m^2$ was applied to all the SFE curves.

It should be noted that the spin-polarization calculations in all the supercells converged to ferromagnetism; therefore, paramagnetic properties were not predicted. As seen in the phase diagram (Figure 8(b)), the Co-Ni alloys are ferromagnetic for quite a wide range of temperatures [67, 68, 69, 70]. Zhang et al. investigated various energy contributions to the SFE of Ni and found that the magnetic contribution to the SFE was not significant (on the order of $1 \, mJ/m^2$) even at the Curie point [38]. First-principles trained cluster expansions utilizing magnetic and compositional degrees of freedom have not yet been fully developed for complex alloys such as the Co-Ni system [71, 72], and the inclusion of the magnetic degree of freedom to model the paramagnetic state in this study would dramatically increase the computation expense beyond what is feasible.

4. Discussion

4.1. Comparison of Stacking Fault Energy Models and Methods

The ANNI model and supercell model for predicting the SFE for pure Co and Ni are comparable and within 5% at elevated temperatures, as shown in Figure 8(c). However, the ANNI model deviates significantly compared to the Ericsson model in the concentrated region, as shown in Figures 11(a) and 12. Such differences arise because the ANNI model neglects the 2^{nd} , 4^{th} , 6^{th} ...

planar interactions and the interfacial effects between ISF and FCC planes, which are captured by the FCC+ISF or tilted supercells. It has been shown by Chandran et al. that the ANNI method is more likely to underestimate the 0 K SFE with increasing Co content compared with supercell method [73]. This could mean that these interactions are non-trivial when solute interactions are involved. In fact, the cluster expansion ECIs of FCC+ISF supercell in Figure 6(b) capture the lattice site interactions between the ISF sites and FCC sites (indicated by black arrows), which is impossible for the FCC or HCP cluster expansions. Therefore, for alloy composition far from dilute region, more sophisticated techniques are required to describe the faulted phase. Natarajan et al. has proposed an approach to calculate the unstable stacking fault energy of concentrated binary alloys [74]. They introduced a glide vector to the supercells that shifted the perfect structures to defected structures. By varying the glide vector magnitude, the stacking fault energy surface along the glide directions can be determined [74]. Colloquially, this method is also called the 'tilted cell' method, which we also used here to compare SFEs of pure Ni and Co. Thus, we believe the SFEs would be very similar between our work and theirs for pure Ni and Co. For alloys, the cluster expansion-based model from Natarajan and Van der Ven can also capture defect-solute interactions. The parent cell configurations may or may not include segregated atoms on certain planes, so this will make it difficult to quantify the effects of segregation. Therefore, the SFE determined from two methods will be different. The main difference might be when segregation takes place – interactions that correlated to segregation are probably lost using the methods outlined in their paper. A more direct supercell method in Chandran et al.'s study employed special quasi-random structures (SQS) to mimic the random distributions of atoms in finite-sized supercells [73]. The SQS method is difficult to be applied to study segregated states but it is expected to be close to the unsegregated SFE in this study.

The influences of $g_{\phi}^{conf.}$ and $g_{\phi}^{vib.}$ on SFE can be analyzed separately. By considering only the configuration contribution, the unsegregated SFE is expected to be invariant with temperature, as we can see the overlap between 570 K and 1170 K unsegregated SFEs shown in Figure 10(c). When segregation occurs, the segregated SFE is always lower than the unsegregated SFE, as seen in Figure 10(c) and Figure 11(a) for the energy difference between segregated and unsegregated SFEs at 570 K or 1170 K. This could be due to that segregation of Co at ISF reduce the SFE of the system. As seen in Figure 8(c) that the segregation excess decreases with increasing temperature, the narrower gap between the segregated and unsegregated SFEs at 1170 K than that at 570 K could be due to the lower extent of Co segregation. By considering the energy difference between the segregated and unsegregated

SFEs with respect to the Co segregation at 1170 K and 570 K, a 1 at.% Co

segregation excess is likely to reduce SFE by 1 to 7 mJ/m^2 . By considering both $g_{\phi}^{conf.}$ and $g_{\phi}^{vib.}$, the SFEs were lowered for the Ni-rich alloys and higher for the Co-rich alloys at 570 K (see Figure 10(a)). Same observations can be made for segregated or unsegregated SFEs at 570 K or 1170 K, see Figure 10(b) and Figure 10(c). For the energy difference between the segregated and unsegregated SFEs at 570 K, vibrational effects tend to narrow this energy difference compared to the abovementioned configurational effects, see red curves in Figure 11(a) and Figure 11(b). In this case, a 1 at.% Co segregation excess is likely to reduce SFE by 0 to $4 mJ/m^2$.

We found that the ISF phase cannot be treated solely as the bulk HCP This is evidenced by comparing the calculated free energy of the "fictitious" ISF phase from Eq.10 and 12b to the predicted free energy of the HCP phase, as shown in Figure 13. The g_{ISF} curve lies above the g_{HCP} curve for concentrated solutions, and the two profiles converge for pure Ni and Co, as shown in Figure 13. As proposed by Ericsson [15], q_{ISF} for the virtual ISF phase represents all the energy contributions of (1) the FCC-to-ISF structural transformation, and (2) the interfacial effects due to chemical fluctuations, including information more than just the FCC-to-HCP phase transformation. For the first term, due to the same structure of the ISF and the HCP phases, this FCC-to-ISF structural transformation is often treated as the FCC-to-HCP phase transformation, which is either calculated by the supercell method or the ANNI model. The tilted supercell method is preferred because the plate-like ISF allow FCC-ISF and FCC-FCC planar interactions and the bulk HCP phase in the ANNI model cannot capture this. This FCC+ISF layer interactions are expected to account for 4 to 8 mJ/m^2 for pure Ni, evaluated from a previous study by Li et al. [36]. For pure Co and Ni, the interfacial energy will be negligible because there are no chemical fluctuations around the ISF. Therefore, the FCC to ISF structural transformation is the major contribution to the free energy of ISF for pure Co and Ni. For the concentrated solution, the interfacial effects is not negligible and it could be the major contribution to the energy difference between the ISF phase and the HCP phase. Due to the fact that chemical fluctuations around the ISF region will also affect the FCC-FCC and FCC-ISF planar interactions, distinguishing their contributions requires performing similar calculations on various FCC+ISF supercells with different FCC and ISF volume fractions.

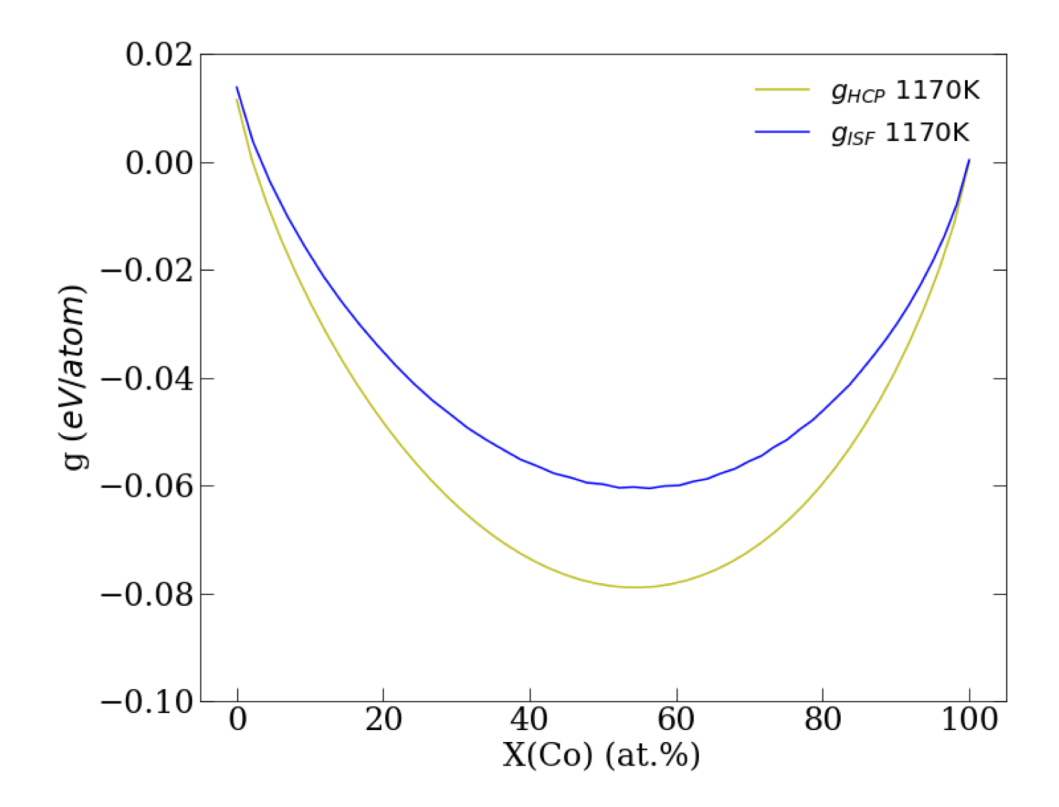


Figure 13: Calculated Gibbs free energies of Co-Ni system ISF and HCP structures.

4.2. Comparison to Experiments

For pure Ni, Section 3.1 has demonstrated that the supercell method is more reliable on predicting the SFE. The most recognized experiment on pure Ni was to directly measure the separation spacing of dissociated partials or faulted dipoles on the (111) glide plane under electron microscopy and calculate the SFE within the anisotropic elasticity theory [59]. Resolving the partials or faulted dipoles under microscope requires extreme care to tilt the specimen into a favored direction and to optimize the beam conditions [59].

For pure Co, Ericsson found that the SFE for the HCP and FCC phases increase linearly with temperature with by $10~mJ/m^2/K$ [66]. However, the HCP and FCC SFEs were discontinuous across the phase transformation temperature at 700 K that the FCC SFE is about $10~mJ/m^2$ and the HCP SFE is about $-20~mJ/m^2/K$ [66]. Linear extrapolation of the FCC Co SFE from elevated temperatures to 0 K leads to a value between -10 to $-5~mJ/m^2/K$. And the linear extrapolation of the HCP Co SFE from elevated temperatures to 0 K leads to a value around $40~mJ/m^2/K$. The FCC SFE of Co cannot be directly compared to the HCP SFE because of the different stacking sequence; therefore, the predicted Co SFE below phase

transformation temperature should be treated carefully.

For non-dilute compositions, experimental measurements of the stacking fault energy of Co-33Ni at elevated temperatures were carried out by Ericsson [66], using the extended dislocation node method [75]. For Co-33Ni, Ericsson determined that the SFE increased by 0.03 $mJ/m^2/K$ from 300 to 823 K, which compares well to our predictions shown in Figure 12. However, only the absolute values of our segregated SFE predictions compared well to the experimental data [66]. In revisiting Ericsson's in-situ experiment, the experiment allowed a 45-min annealing at each temperature before measurements and observed node shrinkage/expansion during heat treatment [66]. This may imply that segregation could occur during the annealing period since segregation is expected to increase stacking fault width by decreasing SFE [76]; however, no measurements on chemical fluctuations have been carried out for this system. Other factors such as thermally activated unpinning of partial dislocations, and change of elastic constants due to temperature change could also influence the area of the stacking fault. Yang and colleagues studied the martensitic transformation of a Co-32Ni alloy [77]. With the similar composition, the low SFE predicted for the Co-33Ni further supports their observation of a large number of stacking faults after annealing [77].

For other concentrated compositions, our predicted segregated SFE at finite temperatures agree with the limited experimental data between 0 at.% and 70 at.% Co but the exact experimental conditions are difficult to track and compare. [73, 66, 76, 78]. The SFE predicted in this study can be further applied to study dislocation evolution and plasticity of this system because quantifying the SFE and the Suzuki segregation from experiments requires extreme care of instrumentalists and good conditions of equipment [59, 66].

4.3. Segregation Isotherm

530

The segregation isotherm is known as follows [79]:

$$\frac{X_{ISF}}{1 - X_{ISF}} = \frac{X_{FCC}}{1 - X_{FCC}} exp\left[-\frac{\Delta E^{seg}}{kT}\right]$$
 (14)

in which ΔE^{seg} is the segregation free energy and k is Boltzmann constant. The segregation free energy can be fitted by using the GCMC predicted X_{ISF} and X_{FCC} . X_{ISF} is evaluated for layer-5 and layer-6 of the 8-layered supercell, and X_{FCC} is evaluated for other FCC layers. The details of fitting ΔE^{seg} can be found in the supplementary Section S6.

The calculated segregation isotherm for Co is shown in Figure 14(a), in which the negative values of segregation free energy corresponds to the

driving force of Co segregation to the stacking fault. We find that the segregation free energy is not temperature dependent, the Arrhenius relation for $\text{Co}_{50}\text{Ni}_{50}$ is shown in Figure 14(b). This implies that calculations made at a single temperature can sufficiently describe the segregation behavior for a given alloy.

In Section 3.1, we determined that the Co solute interaction energy is about -33.5 meV/solute, and it is shown as the blue line in Figure 14(a). The segregation free energy deviates from the compositionally-independent interaction energy. As described by Ma et al [80], The interaction energy is a first-order approximation of the segregation driving force and only partially describes the full free energy. For example, Rao et al. found that the interaction energy of Cr is positive in the superlattice intrinsic stacking fault (SISF) of γ' Ni₃Al [10]; and a recent study by Feng et al. found that Co lowered the interaction energy by strengthening the Co-Cr bonding in the SISF [34]. The segregation free energy is expected to deviate from the interaction energy due to factors such as preferred bondings and concentrated effects. Our predicted segregation free energy implicitly includes other contributions, such as the configurational entropy of mixing and the planar-dependent free energy of mixing in the vicinity of the ISF at finite concentrations, which can be accounted for using thermodynamic modeling of bulk phases [80]. However, we reiterate that the ISF phase cannot be treated as a bulk phase, as shown by the discrepancy in the free energies between our calculated free energy of the ISF phase compared to the bulk HCP phase in Figure 13.

Because a more negative segregation energy leads to stronger segregation, the Co interaction energy will predict stronger Co segregation between 0 to 25 at.% and 88 at.% to 100 at.% Co, and predict lower Co segregation between 25 at.% and 88 at.%, compared to the GCMC segregation free energy, see Figure 14. The Co segregation predicted at different temperatures shown in Figure 8(c) all correspond to the GCMC ΔE_{seg} in Figure 14(a).

Although the influence of ferro-to-para magnetic transformation on stacking fault calculation is expected to be small in pure Ni [38], the paramagnetic states in this system remains unknown and are difficult to model quantitatively. Therefore, care should be taken to compare the results above the Curie temperatures.

To compare the above segregation energy with a typical grain boundary (GB) or free surfaces segregation in the Ni alloy system, segregation energy of ISF is one or two order of magnitude smaller than the grain boundary or free surface segregation energies [81]. For 3d metals on (111) free surfaces of FCC Ni, Ti and Cr have the highest segregation energies of -750 meV/atom and -800 meV/atom, respectively, and the Co surface segregation energy on (111) plane is -130 meV/atom [82]. For 3d metals on Ni Σ 5(210) GB, segregation

of Ti and V is likely to strengthen the GB through lowering the GB energy by 500 meV/atom, and Co is not likely to strengthen or weaken the GB [83]. In the CoNi superalloys, Co was found to be exclusively segregate to SISFs in the γ' phase [6, 21, 32, 33, 34, 35], and Feng et al. calculated the segregation free energy of Co in SISF about -20 meV when the Co concentration in the bulk γ' phase is around 6.6 at.% from experiments [34], comparable to the calculated segregation free energy -18.5 meV for this FCC Co-Ni system at the same Co concentration. This ISF segregation, together with other interfacial segregation, is key to develop a comprehensive knowledge of the mechanical properties of an alloy system for alloy design.

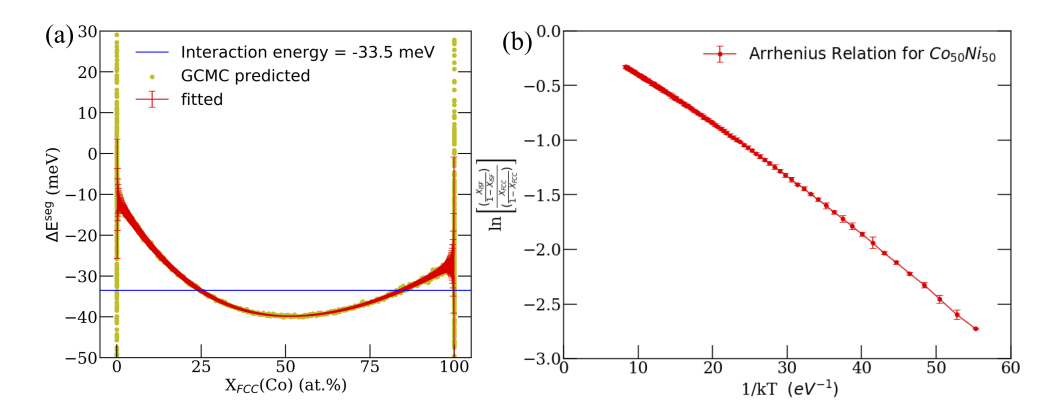


Figure 14: (a) Segregation energy of the Co-Ni FCC+ISF system. Horizontal blue line denotes the interaction energy of Co. (b) Arrhenius relationship for segregation isotherm of $Co_{50}Ni_{50}$ alloy.

5. Conclusions

We studied the segregation of Co to stacking faults in Co-Ni binary alloys through first-principles calculations, cluster expansions, and Monte Carlo simulations. We coupled the supercell approach with the Ericsson model to quantitatively predict the stacking fault energies when segregation at intrinsic stacking faults occurs. The method developed in this study could be leveraged to study the solute segregation behaviors in interfacial problems such as stacking faults, grain boundary and dislocation of similar systems. The main conclusions are listed below:

- At all modeled temperatures between 200 K and 1500 K, Co was predicted to always segregate exclusively to the two innermost atomic planes of the ISF. The extent of segregation peaks at approximately 50 at.% Co and decreases in both the Co-lean and Co-rich regions.
- Both the supercell method and the ANNI model predicted comparable SFEs for pure Co and Ni at 0 K and elevated temperatures. For the concen-

- trated compositions, ANNI model underestimates the SFE by more than 50 mJ/m^2 compared with Ericsson model. Compared with limited experimental data of Co-33Ni, the Ericsson SFE agrees with the experimental values when segregation is considered, which implies that solute segregation could happen during experimental measurements.
 - By considering Co segregation in SFE calculation using Ericsson model, $g_{\phi}^{conf.}$ and $g_{\phi}^{vib.}$ behaves differently: (1) configurational entropy tends to increase the SFE with increasing temperature, meanwhile the vibrational entropy increases the SFE of Co-rich compositions but decreases, slightly, the SFE of Ni-rich compositions with increasing temperature. (2) considering only $g_{\phi}^{conf.}$, 1 at.% Co segregation in the ISF leads to 1 to $7~mJ/m^2$ decrease in SFE compared with the unsegregated state. (3) considering both $g_{\phi}^{conf.}$ and $g_{\phi}^{vib.}$, 1 at.% Co segregation in the ISF leads to 0 to 4 mJ/m^2 decrease in SFE compared with the unsegregated state.
 - The difference between free energy of a "standalone" ISF and that of a bulk HCP phase emphasizes that the bulk hcp phase cannot be considered as the ISF phase. This energy difference can be attributed to the FCC+ISF layer interactions and interfacial energy calculated through the Ericsson model.
 - The segregation behavior of Co in the ISF follows the segregation free energy determined by GCMC simulations. The GCMC segregation energy is temperature-invariant and negative across the whole composition range. Compared with the Co interaction energy -33 meV, the GCMC segregation free energy is higher between 0 to 25 at.% Co and 88 at.% to 100 at.%, and lower between 25 at.% to 100 at.% Co.

Appendix A. Calculation of Stacking Fault Energy.

655

Eq.12(a) provides a general expression for stacking fault energy, but the expression for g_{ISF} provided in Eq.12(b) cannot be used because ϵ and ω are not known a priori. The free energy of the ISF structure $g_{ISF}(X_{ISF})$ can be directly obtained from Eq.10, where $g_{FCC+ISF}(X_{tot})$ and $g_{FCC}(X_{FCC})$ are from integrating the chemical potential obtained from GCMC simulations on the FCC+ISF and FCC structures, respectively. The compositions X_{ISF} , X_{FCC} , and X_{tot} are extracted from the point correlation functions in the FCC+ISF GCMC simulations. Also, in the FCC+ISF GCMC simulations, the Suzuki criterion is inherently satisfied (Eq.11) and the tangents of the FCC free energy curves can be determined to obtain μ_{FCC}^{Co} and μ_{FCC}^{Ni} as a function of FCC concentration. With $g_{ISF}(X_{ISF})$, $g_{FCC}(X_{FCC})$, μ_{FCC}^{Co} and

 μ_{FCC}^{Ni} , the segregated SFE can be written as:

$$\gamma_m^{seg.}(X_{FCC}) = g_{ISF}(X_{ISF}) - \mu_{FCC}^{Co}(X_{FCC})X_{ISF} - \mu_{FCC}^{Ni}(X_{FCC})(1 - X_{ISF})$$
(Appendix .1)

And the unsegregated SFE can be written as:

$$\gamma_m^{unseg.}(X_{FCC}) = g_{ISF}(X_{FCC}) - \mu_{FCC}^{Co}(X_{FCC}) X_{FCC} - \mu_{FCC}^{Ni}(X_{FCC}) (1 - X_{FCC})$$

$$= g_{ISF}(X_{FCC}) - g_{FCC}(X_{FCC}) \qquad (Appendix .2)$$

Acknowledgement

This material is based upon work supported by the National Science Foundation under Grant No. (CAREER DMR-1848128). The authors would additionally like to acknowledge Purdue University for supporting this work through start-up funds. This research was supported in part through computational resources provided by Information Technology at Purdue, West Lafayette, Indiana. The authors would like to thank Longsheng Feng and Prof. Yunzhi Wang in Ohio State University for thorough discussions on segregation isotherm.

References

670

675

- Z. Li, K. G. Pradeep, Y. Deng, D. Raabe, C. C. Tasan, Metastable high-entropy dual-phase alloys overcome the strength-ductility tradeoff, Nature 534 (2016) 227.
 URL https://doi.org/10.1038/nature17981
- [2] G. Laplanche, A. Kostka, C. Reinhart, J. Hunfeld, G. Eggeler, E. George, Reasons for the superior mechanical properties of mediumentropy CrCoNi compared to high-entropy CrMnFeCoNi, Acta Materialia 128 (2017) 292–303.
- [3] C. Niu, C. R. LaRosa, J. Miao, M. J. Mills, M. Ghazisaeidi, Magnetically-driven phase transformation strengthening in high entropy alloys, Nature Communications 9 (1) (Dec. 2018). doi:10.1038/ s41467-018-03846-0.
 - URL http://www.nature.com/articles/s41467-018-03846-0
- [4] A. Suzuki, T. M. Pollock, High-temperature strength and deformation of γ/γ' two-phase Co–Al–W-base alloys, Acta Materialia 56 (6) (2008) 1288–1297.

- [5] V. Vorontsov, L. Kovarik, M. Mills, C. Rae, High-resolution electron microscopy of dislocation ribbons in a CMSX-4 superalloy single crystal, Acta Materialia 60 (12) (2012) 4866–4878.
 - [6] M. S. Titus, A. Mottura, G. Babu Viswanathan, A. Suzuki, M. J. Mills, T. M. Pollock, High resolution energy dispersive spectroscopy mapping of planar defects in L12-containing Co-base superalloys, Acta Materialia 89 (2015) 423-437. doi:10.1016/j.actamat.2015.01.050. URL https://linkinghub.elsevier.com/retrieve/pii/S1359645415000634

695

- [7] M. S. Titus, Y. M. Eggeler, A. Suzuki, T. M. Pollock, Creep-induced planar defects in L12-containing Co-and CoNi-base single-crystal superalloys, Acta Materialia 82 (2015) 530–539.
 - [8] J. Ding, Q. Yu, M. Asta, R. O. Ritchie, Tunable stacking fault energies by tailoring local chemical order in crooni medium-entropy alloys, Proceedings of the National Academy of Sciences 115 (36) (2018) 8919-8924. arXiv:https://www.pnas.org/content/115/36/ 8919.full.pdf, doi:10.1073/pnas.1808660115. URL https://www.pnas.org/content/115/36/8919
 - [9] C. Slone, J. Miao, E. George, M. Mills, Achieving ultra-high strength and ductility in equiatomic CrCoNi with partially recrystallized microstructures, Acta Materialia 165 (2019) 496–507.
- [10] Y. Rao, T. Smith, M. Mills, M. Ghazisaeidi, Segregation of alloying elements to planar faults in γ' -Ni3Al, Acta Materialia 148 (2018) 173–184.
- [11] Y. Ikeda, F. Körmann, I. Tanaka, J. Neugebauer, Impact of chemical fluctuations on stacking fault energies of CrCoNi and CrMnFeCoNi high entropy alloys from first principles, Entropy 20 (9) (2018) 655.
 - [12] B. Gludovatz, A. Hohenwarter, K. V. S. Thurston, H. Bei, Z. Wu, E. P. George, R. O. Ritchie, Exceptional damage-tolerance of a mediumentropy alloy CrCoNi at cryogenic temperatures, Nature Communications 7 (2016) 10602.
- URL https://doi.org/10.1038/ncomms10602
 - [13] H. Suzuki, Chemical interaction of solute atoms with dislocations, Science reports of the Research Institutes, Tohoku University. Ser. A, Physics, chemistry and metallurgy 4 (1952) 455–463.

- [14] H. Suzuki, Segregation of solute atoms to stacking faults, Journal of the Physical Society of Japan 17 (2) (1962) 322–325.
 - [15] T. Ericsson, On the Suzuki effect and spinodal decomposition, Acta Metallurgica 14 (9) (1966) 1073–1084.
 - [16] J. Hirth, Thermodynamics of stacking faults, Metallurgical Transactions 1 (9) (1970) 2367.
- Y. Koizumi, T. Nukaya, S. Suzuki, S. Kurosu, Y. Li, H. Matsumoto, K. Sato, Y. Tanaka, A. Chiba, Suzuki segregation in Co-Ni-based superalloy at 973 K: An experimental and computational study by phase-field simulation, Acta Materialia 60 (6-7) (2012) 2901–2915.
- [18] M. S. Titus, R. K. Rhein, P. B. Wells, P. C. Dodge, G. B. Viswanathan,
 M. J. Mills, A. Van der Ven, T. M. Pollock, Solute segregation and deviation from bulk thermodynamics at nanoscale crystalline defects,
 Science advances 2 (12) (2016) e1601796.
 - [19] J. Gazquez, M. Coll, N. Roma, F. Sandiumenge, T. Puig, X. Obradors, Structural defects in trifluoroacetate derived YBa2Cu3O7 thin films, Superconductor Science and Technology 25 (6) (2012) 065009.

- [20] C. P. Poole Jr, H. A. Farach, Superconductivity, Encyclopedia of Inorganic and Bioinorganic Chemistry (2011).
- [21] Y. Eggeler, J. Müller, M. Titus, A. Suzuki, T. Pollock, E. Spiecker, Planar defect formation in the γ' phase during high temperature creep in single crystal CoNi-base superalloys, Acta Materialia 113 (2016) 335–349.
 - [22] H. Saka, Experimental evidence for Suzuki segregation to the stacking fault of an extended dislocation in a Cu-Si alloy, Philosophical Magazine A 47 (1) (1983) 131–140.
- ⁴⁵ [23] T. Kamino, Y. Ueki, H. Hamajima, K. Sasaki, K. Kuroda, H. Saka, Direct evidence for Suzuki segregation obtained by high-resolution analytical electron microscopy, Philosophical magazine letters 66 (1) (1992) 27–31.
- [24] B. G. Mendis, I. P. Jones, R. E. Smallman, Suzuki segregation in a binary Cu-Si alloy, Journal of electron microscopy 53 (4) (2004) 311–323.

- [25] J. Justo, T. Schmidt, A. Fazzio, A. Antonelli, Segregation of dopant atoms on extended defects in semiconductors, Physica B: Condensed Matter 302 (2001) 403–407.
- properties of metal impurities at dislocations in silicon, physica status solidi (a) 202 (5) (2005) 911–920.
 - [27] Y. Ohno, Y. Tokumoto, I. Yonenaga, Doping effects on the stability of stacking faults in silicon crystals, Thin Solid Films 520 (8) (2012) 3296–3299.

- [28] Y. Ohno, T. Taishi, Y. Tokumoto, I. Yonenaga, Interaction of dopant atoms with stacking faults in silicon crystals, Journal of Applied Physics 108 (7) (2010) 073514.
- [29] J. Nie, K. Oh-Ishi, X. Gao, K. Hono, Solute segregation and precipitation in a creep-resistant Mg–Gd–Zn alloy, Acta Materialia 56 (20) (2008) 6061–6076.
 - [30] J. Nie, Y. Zhu, J. Liu, X.-Y. Fang, Periodic segregation of solute atoms in fully coherent twin boundaries, Science 340 (6135) (2013) 957–960.
- [31] T. F. Kelly, M. K. Miller, Atom probe tomography, Review of Scientific Instruments 78 (3) (2007) 031101.
 - [32] G. Viswanathan, R. Shi, A. Genc, V. Vorontsov, L. Kovarik, C. Rae, M. Mills, Segregation at stacking faults within the γ' phase of two Nibase superalloys following intermediate temperature creep, Scripta Materialia 94 (2015) 5–8.
- [33] T. M. Smith, B. Good, T. Gabb, B. Esser, A. Egan, L. Evans, D. Mc-Comb, M. Mills, Effect of stacking fault segregation and local phase transformations on creep strength in ni-base superalloys, Acta Materialia 172 (2019) 55–65.
- [34] L. Feng, Y. Rao, M. Ghazisaeidi, M. J. Mills, Y. Wang, Quantitative prediction of suzuki segregation at stacking faults of the γ 'phase in nibase superalloys, Acta Materialia 200 (2020) 223–235.
 - [35] D. Barba, A. J. Egan, Y. Gong, M. J. Mills, R. C. Reed, Rationalisation of the micromechanisms behind the high-temperature strength limit in single-crystal nickel-based superalloys, in: Superalloys 2020, Springer, 2020, pp. 260–272.

[36] R. Li, S. Lu, D. Kim, S. Schönecker, J. Zhao, S. K. Kwon, L. Vitos, Stacking fault energy of face-centered cubic metals: thermodynamic and ab initio approaches, Journal of Physics: Condensed Matter 28 (39) (2016) 395001. doi:10.1088/0953-8984/28/39/395001. URL https://iopscience.iop.org/article/10.1088/0953-8984/28/39/395001

790

- [37] P. Denteneer, W. Van Haeringen, Stacking-fault energies in semiconductors from first-principles calculations, Journal of Physics C: Solid State Physics 20 (32) (1987) L883.
- 795 [38] X. Zhang, B. Grabowski, F. Körmann, A. V. Ruban, Y. Gong, R. C. Reed, T. Hickel, J. Neugebauer, Temperature dependence of the stacking-fault Gibbs energy for Al, Cu, and Ni, Physical Review B 98 (22) (2018) 224106. doi:10.1103/PhysRevB.98.224106. URL https://link.aps.org/doi/10.1103/PhysRevB.98.224106
- [39] A. Breidi, J. Allen, A. Mottura, First-principles calculations of thermodynamic properties and planar fault energies in Co₃ X and Ni₃ X L1₂ compounds: Thermodynamic properties and planar fault energies in Co₃X and Ni₃X, physica status solidi (b) 254 (9) (Sep. 2017). doi:10.1002/pssb.201600839.
 URL http://doi.wiley.com/10.1002/pssb.201600839
 - [40] A. Breidi, J. Allen, A. Mottura, First-principles modeling of superlattice intrinsic stacking fault energies in Ni3Al based alloys, Acta Materialia 145 (2018) 97–108. doi:10.1016/j.actamat.2017.11.042. URL https://linkinghub.elsevier.com/retrieve/pii/ S1359645417309850
 - [41] CASM Developers, Casmcode: V0.2.1 (Apr. 2017). doi:10.5281/zenodo.546148.
 URL https://zenodo.org/record/546148
 - [42] J. M. Sanchez, F. Ducastelle, D. Gratias, Generalized cluster description of multicomponent systems, Physica A: Statistical Mechanics and its Applications 128 (1-2) (1984) 334–350.
 - [43] B. Puchala, A. Van der Ven, Thermodynamics of the Zr-O system from first-principles calculations, Physical Review B 88 (9) (2013) 094108.
- [44] G. L. Hart, V. Blum, M. J. Walorski, A. Zunger, Evolutionary approach for determining first-principles hamiltonians, Nature materials 4 (5) (2005) 391.

- [45] M. Stone, Cross-validation: A review, Statistics: A Journal of Theoretical and Applied Statistics 9 (1) (1978) 127–139.
- [46] A. van de Walle, G. Ceder, Automating first-principles phase diagram calculations, Journal of Phase Equilibria 23 (4) (2002) 348.
 - [47] A. Van de Walle, M. Asta, Self-driven lattice-model Monte Carlo simulations of alloy thermodynamic properties and phase diagrams, Modelling and Simulation in Materials Science and Engineering 10 (5) (2002) 521.
 - [48] A. Togo, I. Tanaka, First principles phonon calculations in materials science, Scripta Materialia 108 (2015) 1–5, publisher: Elsevier.

- [49] L. Chaput, A. Togo, I. Tanaka, G. Hug, Phonon-phonon interactions in transition metals, Physical Review B 84 (9) (2011) 094302. doi: 10.1103/PhysRevB.84.094302. URL https://link.aps.org/doi/10.1103/PhysRevB.84.094302
- [50] W. Kohn, L. J. Sham, Self-consistent equations including exchange and correlation effects, Physical review 140 (4A) (1965) A1133.
 - [51] G. Kresse, J. Furthmüller, Efficient iterative schemes for ab initio totalenergy calculations using a plane-wave basis set, Physical review B 54 (16) (1996) 11169.
- [52] G. Kresse, D. Joubert, From ultrasoft pseudopotentials to the projector augmented-wave method, Physical Review B 59 (3) (1999) 1758.
 - [53] P. E. Blöchl, Projector augmented-wave method, Physical review B 50 (24) (1994) 17953.
- [54] J. P. Perdew, K. Burke, M. Ernzerhof, Generalized gradient approximation made simple, Physical review letters 77 (18) (1996) 3865.
 - [55] H. J. Monkhorst, J. D. Pack, Special points for Brillouin-zone integrations, Physical review B 13 (12) (1976) 5188.
 - [56] M. Methfessel, A. Paxton, High-precision sampling for Brillouin-zone integration in metals, Physical Review B 40 (6) (1989) 3616.
- [57] P. E. Blöchl, O. Jepsen, O. K. Andersen, Improved tetrahedron method for brillouin-zone integrations, Phys. Rev. B 49 (1994) 16223-16233. doi:10.1103/PhysRevB.49.16223. URL https://link.aps.org/doi/10.1103/PhysRevB.49.16223

- [58] S. Shang, W. Wang, Y. Wang, Y. Du, J. Zhang, A. Patel, Z. Liu,
 Temperature-dependent ideal strength and stacking fault energy of fcc
 ni: a first-principles study of shear deformation, Journal of Physics:
 Condensed Matter 24 (15) (2012) 155402.
- [59] C. B. Carter, S. M. Holmes, The stacking-fault energy of nickel, The Philosophical Magazine: Α Journal of Theoretical Experimental and Applied Physics 35 (5) (1977) 1161–1172. 860 doi:10.1080/14786437708232942. URL https://www.tandfonline.com/doi/full/10.1080/ 14786437708232942
- [60] L.-Y. Tian, R. Lizárraga, H. Larsson, E. Holmström, L. Vitos, A first principles study of the stacking fault energies for fcc Co-based binary alloys, Acta Materialia 136 (2017) 215-223. doi:10.1016/j.actamat.2017.07.010. URL https://linkinghub.elsevier.com/retrieve/pii/S1359645417305608
- [61] T. L. Achmad, W. Fu, H. Chen, C. Zhang, Z.-G. Yang, Computational thermodynamic and first-principles calculation of stacking fault energy on ternary Co-based alloys, Computational Materials Science 143 (2018) 112–117. doi:10.1016/j.commatsci.2017.11.004.

 URL https://linkinghub.elsevier.com/retrieve/pii/S0927025617306225
 - [62] A. Zunger, S.-H. Wei, L. G. Ferreira, J. E. Bernard, Special quasir-andom structures, Phys. Rev. Lett. 65 (1990) 353-356. doi:10.1103/PhysRevLett.65.353.
 URL https://link.aps.org/doi/10.1103/PhysRevLett.65.353
- 63] A. Van de Walle, P. Tiwary, M. De Jong, D. Olmsted, M. Asta, A. Dick, D. Shin, Y. Wang, L.-Q. Chen, Z.-K. Liu, Efficient stochastic generation of special quasirandom structures, Calphad 42 (2013) 13–18.
 - [64] A. Mottura, A. Janotti, T. M. Pollock, A first-principles study of the effect of ta on the superlattice intrinsic stacking fault energy of l12-co3 (al, w), Intermetallics 28 (2012) 138–143.

[65] K. Wertz, D. Weaver, D. Wen, M. S. Titus, R. Shivpuri, S. R. Niezgoda, M. J. Mills, S. L. Semiatin, Supersolvus hot workability and dynamic recrystallization in wrought co-al-w-base alloys, in: Superalloys 2020, Springer, 2020, pp. 857–869.

- [66] T. Ericsson, The temperature and concentration dependence of the stacking fault energy in the Co-Ni system, Acta Metallurgica 14 (7) (1966) 853-865. doi:10.1016/0001-6160(66)90006-X.

 URL https://linkinghub.elsevier.com/retrieve/pii/000161606690006X
- [67] P. Söderlind, O. Eriksson, B. Johansson, R. Albers, A. Boring, Spin and orbital magnetism in Fe-Co and Co-Ni alloys, Physical Review B 45 (22) (1992) 12911.
- [68] H. P. Myers, W. Sucksmith, The spontaneous magnetization of cobalt, Proceedings of the Royal Society of London. Series A.
 Mathematical and Physical Sciences 207 (1091) (1951) 427-446. doi:10.1098/rspa.1951.0132.
 URL http://www.royalsocietypublishing.org/doi/10.1098/rspa.1951.0132
- [69] J. Crangle, G. M. Goodman, The Magnetization of Pure Iron and Nickel, Proceedings of the Royal Society A: Mathematical, Physical and Engineering Sciences 321 (1547) (1971) 477–491. doi:10.1098/rspa.1971.0044.

 URL http://rspa.royalsocietypublishing.org/cgi/doi/10.1098/rspa.1971.0044
- 910 [70] H. Okamoto, M. Schlesinger, E. Mueller (Eds.), Alloy Phase Diagrams, ASM International, 2016. doi:10.31399/asm.hb.v03.9781627081634. URL https://dl.asminternational.org/books/book/36/alloy-phase-diagrams
- [71] I. Abrikosov, A. Ponomareva, P. Steneteg, S. Barannikova, B. Alling,
 Recent progress in simulations of the paramagnetic state of magnetic
 materials, Current Opinion in Solid State and Materials Science 20 (2)
 (2016) 85–106. doi:10.1016/j.cossms.2015.07.003.
 URL https://linkinghub.elsevier.com/retrieve/pii/
 S1359028615300048
- [72] M. Lavrentiev, S. Dudarev, D. Nguyen-Manh, Magnetic cluster expansion simulations of FeCr alloys, Journal of Nuclear Materials 386-388 (2009) 22-25. doi:10.1016/j.jnucmat.2008.12.052.

 URL https://linkinghub.elsevier.com/retrieve/pii/S0022311508007940

- [73] M. Chandran, S. K. Sondhi, First-principle calculation of stacking fault energies in Ni and Ni-Co alloy, Journal of Applied Physics 109 (10) (2011) 103525. doi:10.1063/1.3585786.

 URL http://aip.scitation.org/doi/10.1063/1.3585786
- [74] A. R. Natarajan, A. Van der Ven, Linking electronic structure calculations to generalized stacking fault energies in multicomponent alloys, npj Computational Materials 6 (1) (2020) 1–9.
 - [75] T. Jossang, M. Stowell, J. Hirth, J. Lothe, On the determination of stacking fault energies from extended dislocation node measurements, Acta metallurgica 13 (3) (1965) 279–291.
- 935 [76] P. Gallagher, The influence of alloying, temperature, and related effects on the stacking fault energy, Metallurgical Transactions 1 (9) (1970) 2429–2461.
- [77] H. Yang, Y. Liu, Factors influencing the stress-induced fcc-hcp martensitic transformation in Co-32Ni single crystal, Acta Materialia 54 (18) (2006) 4895-4904. doi:10.1016/j.actamat.2006.06.047.

 URL https://linkinghub.elsevier.com/retrieve/pii/S1359645406004678
- [78] L. Rémy, A. Pineau, В. Thomas, Temperature dependence stacking fault energy in close-packed metals and Materials Science and Engineering 36 (1) (1978)945 doi:https://doi.org/10.1016/0025-5416(78)90194-5. URL http://www.sciencedirect.com/science/article/pii/ 0025541678901945
- [79] J. W. Cahn, The impurity-drag effect in grain boundary motion, Acta Metallurgica 10 (9) (1962) 789-798. doi:10.1016/0001-6160(62) 90092-5.

 URL https://linkinghub.elsevier.com/retrieve/pii/0001616062900925
- [80] N. Ma, S. Dregia, Y. Wang, Solute segregation transition and drag force on grain boundaries, Acta Materialia 51 (13) (2003) 3687-3700. doi:10.1016/S1359-6454(03)00184-8. URL https://linkinghub.elsevier.com/retrieve/pii/S1359645403001848
- [81] P. Lejček, M. Šob, V. Paidar, Interfacial segregation and grain boundary embrittlement: An overview and critical assessment of experimental

data and calculated results, Progress in Materials Science 87 (2017) 83-139. doi:10.1016/j.pmatsci.2016.11.001. URL https://linkinghub.elsevier.com/retrieve/pii/S0079642516300755

- ⁵⁶⁵ [82] A. Ruban, H. L. Skriver, J. K. Nørskov, Surface segregation energies in transition-metal alloys, Physical review B 59 (24) (1999) 15990.
 - [83] W. Geng, A. J. Freeman, G. Olson, Influence of alloying additions on grain boundary cohesion of transition metals: First-principles determination and its phenomenological extension, Physical review B 63 (16) (2001) 165415.